Dynamic band collapse in photonic graphene

2013 New J. Phys. 15 013012

(http://iopscience.iop.org/1367-2630/15/1/013012)

New Journal of Physics
The open access journal for physics

Dynamic band collapse in photonic graphene

Andrea Crespi, Giacomo Corrielli, Giuseppe Della Valle, Roberto Osellame[1] and Stefano Longhi

Istituto di Fotonica e Nanotecnologie, Consiglio Nazionale delle Ricerche and Dipartimento di Fisica, Politecnico di Milano, Piazza Leonardo da Vinci 32, I-20133 Milan, Italy
E-mail: roberto.osellame@polimi.it

New Journal of Physics **15** (2013) 013012 (12pp)
Received 12 September 2012
Published 9 January 2013
Online at http://www.njp.org/
doi:10.1088/1367-2630/15/1/013012

Abstract. The band structure and the transport properties of graphene are known to be deeply modified by strong electromagnetic fields. Here we experimentally demonstrate, using an engineered optical waveguide lattice as a model system for ac-driven graphene, the partial and complete collapse of valence and conduction quasi-energy bands corresponding to linearly- and circularly-polarized monochromatic light irradiation, respectively.

Contents

1. Introduction 2
2. Quasi-energy bands in ac-driven honeycomb lattices: partial and complete band collapse 3
3. Ac-driven photonic graphene 6
4. Experimental results 8
5. Conclusions 10
Acknowledgments 11
References 11

[1] Author to whom any correspondence should be addressed.

1. Introduction

Electronic transport in monolayer graphite sheets (graphene) has attracted great interest in recent years [1]. Owing to the honeycomb structure of the crystal lattice, graphene exhibits energy bands with Dirac cones, where the energy-momentum dispersion is linear. This feature is responsible for a strikingly different electronic behaviour as compared to the conventional two-dimensional (2D) electron gases as, for example, in semiconductor heterostructures. At a Dirac point, electrons behave effectively as relativistic massless Dirac fermions, a circumstance that has led to the observation of condensed-matter analogues of the physics of relativistic electrons, such as Klein tunnelling and Zitterbewegung (see, for instance, [2–4]). Several recent works have suggested the possibility of engineering the band structure and the electronic transport properties in graphene by application of electric and/or magnetic fields [4–18], for example to open dynamic band gaps. This has lead to the prediction of a variety of phenomena, such as the photovoltaic Hall effect [7], metal–insulator transition [8], valley-polarized currents in both monolayer and bilayer graphene [9, 10], and the photoinduced quantum Hall effect in the absence of magnetic fields [11]. Remarkably, an ac field can induce dynamic and controllable band gaps in the quasi-energy spectrum of graphene, depending on the strength and polarization of the field. For a linearly polarized field, the anisotropic quasienergy spectrum shows dynamical gaps at non-zero momentum only in certain directions, and no gap is induced at the Dirac point. For a circularly polarized field, a band-gap at the Dirac point can be realized, along with dynamical gaps at other momenta, all of which are tunable by the field intensity [15]. Moreover, partial band collapse can be realized at strong driving fields, in such a way that the valence and conduction bands become flat [15]. Most of such phenomena, however, have not been observed yet.

A highly flexible approach to studying condensed-matter phenomena is the use of accessible model systems with controllable parameters. As a matter of fact, many interesting phenomena in graphene structures are generic to honeycomb lattices and hence they are found in such diverse systems as cold atoms in optical lattices [19–21], electromagnetic waves in photonic lattices [22–26] and sound waves in acoustic crystals [27]. For example, the creation of Dirac points with adjustable properties in a tunable honeycomb optical lattice has been demonstrated recently using ultracold atoms trapped in the periodic potential of interfering laser beams [21], whereas strong edge effects on the pseudodiffusive transport have been observed in photonic graphene [25]. Matter waves in suitably driven optical lattices and light propagation in engineered waveguide lattices have also provided experimentally accessible systems to demonstrate tunnelling control and quasi-energy band engineering in ac-driven 2D or three-dimensional (3D) lattice models [28–30]. In particular, the demonstration of complete band collapse (dynamic localization [31, 32]) in 2D triangular photonic lattices has been reported in [28, 30] exploiting specially-tailored non-monochromatic and linearly-polarized field profiles.

In this work we suggest and demonstrate partial and complete quasi-energy band collapse in honeycomb lattices driven by linearly- and circularly-polarized monochromatic fields. Experimental validation is achieved in a photonic model based on light transport in femtosecond-laser-written waveguide arrays. As for a linearly-polarized field, only partial band collapse can be realized [15]. Here we show that a complete band collapse, corresponding to a frozen dynamic, can be realized using a monochromatic *circularly-polarized* field. In an optical waveguide setting, the effects of external forces can be mimicked by non-inertial forces,

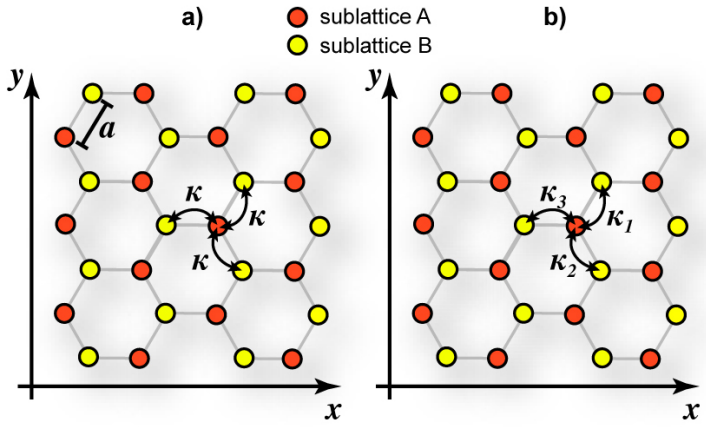

Figure 1. (a) Schematic of a honeycomb lattice, composed of two sublattices A and B, driven by a sinusoidal field $\mathbf{E}(t)$, and (b) effective lattice model with re-normalized hopping amplitudes.

obtained by translating or rotating the waveguides about the propagation direction [33–35]. In particular, the experimental demonstration of non-inertial effects for light waves in a rotating waveguide array was reported in [35]. In the photonic model employed here, linearly- and circularly-polarized electric fields are implemented by translating (rather than rotating) the waveguide arrays in three-dimensions. This is a unique capability of femtosecond laser waveguide writing, which is fully exploited in this work.

2. Quasi-energy bands in ac-driven honeycomb lattices: partial and complete band collapse

Let us consider a planar honeycomb lattice (figure 1(a)), which is composed of two sublattices A and B, as in the single-layer graphene. The coherent motion of an electron hopping between the nearest neighbour sites from different sublattices and driven by an external sinusoidal field $\mathbf{E}(t)$ of frequency ω, in the absence of electron–electron interactions, is described by the tight-binding Hamiltonian

$$\hat{H}(t) = -\hbar\kappa \sum_{\langle n,m\rangle} \left(\hat{c}_n^{\dagger}\hat{c}_m + \hat{c}_m^{\dagger}\hat{c}_n\right) + e\mathbf{E}(t)\cdot\sum_n \mathbf{r}_n\hat{c}_n^{\dagger}\hat{c}_n, \tag{1}$$

where $\hat{c}_n^{\dagger}$ ($\hat{c}_n$) creates (annihilates) an electron at site n and κ is the intersite hopping amplitude between the nearest neighbours $\langle n, m\rangle$. For an arbitrary polarization state, the applied sinusoidal field is given by

$$\begin{aligned}\mathbf{E}(t) &= E_x(t)\mathbf{u}_x + E_y(t)\mathbf{u}_y \\ &= A_x\cos(\omega t+\varphi)\mathbf{u}_x + A_y\cos(\omega t)\mathbf{u}_y.\end{aligned} \tag{2}$$

Linear polarization is attained for $\varphi = 0, \pi$, whereas a circularly-polarized field is obtained for $\varphi = \pm\pi/2$. Owing to the time periodicity of the Hamiltonian $\hat{H}(t)$, the usual energy bands of graphene for the undriven electron are replaced by the quasi-energy bands $\epsilon(\mathbf{k})$, which can be numerically computed by application of the Floquet theory [32]. Here we focus our analysis on the high-frequency regime, corresponding to $\omega \gg \kappa$, where the quasi-energy bands can

be determined from an effective static tight-binding Hamiltonian with renormalized hopping amplitudes (see, for instance, [15, 36, 37]). The effective Hamiltonian reads

$$\hat{H}_{\rm eff} = -\hbar \sum_{\langle n,m \rangle} \left(\kappa_{n,m} \hat{c}_n^\dagger \hat{c}_m + \kappa_{n,m}^* \hat{c}_m^\dagger \hat{c}_n \right), \tag{3}$$

where

$$\kappa_{n,m} = \kappa \left\langle \exp\left[\mathrm{i} \frac{e}{\hbar} (\mathbf{r}_n - \mathbf{r}_m) \cdot \int_0^t \mathrm{d}t' \mathbf{E}(t') \right] \right\rangle \tag{4}$$

and $\langle \cdots \rangle$ denotes the time average over the oscillation cycle $2\pi/\omega$ of the ac field. For the honeycomb lattice and for a generic polarization state of the sinusoidal field, the effective static lattice model, described by the Hamiltonian (3), is shown in figure 1(b). As a result of the ac field, the hopping rate of the electron among nearest neighbour sites is now anisotropic. The renormalized hopping amplitudes κ_1, κ_2 and κ_3 shown in figure 1(b), read explicitly

$$\kappa_1 = \kappa J_0(\Gamma_1) \exp\left[-\mathrm{i} \frac{ea}{2\hbar\omega} A_x \sin\varphi \right], \tag{5}$$

$$\kappa_2 = \kappa J_0(\Gamma_2) \exp\left[-\mathrm{i} \frac{ea}{2\hbar\omega} A_x \sin\varphi \right], \tag{6}$$

$$\kappa_3 = \kappa J_0(\Gamma_3) \exp\left[\mathrm{i} \frac{ea}{\hbar\omega} A_x \sin\varphi \right], \tag{7}$$

where we have set

$$\Gamma_1 = \frac{ea}{2\hbar\omega} \sqrt{A_x^2 \sin^2\varphi + (\sqrt{3}A_y + A_x \cos\varphi)^2}, \tag{8}$$

$$\Gamma_2 = \frac{ea}{2\hbar\omega} \sqrt{A_x^2 \sin^2\varphi + (\sqrt{3}A_y - A_x \cos\varphi)^2}, \tag{9}$$

$$\Gamma_3 = \frac{ea A_x}{\hbar\omega} \tag{10}$$

and $J_0(\Gamma)$ is the Bessel function of first kind and zero order. The corresponding quasi-energy bands can be readily obtained from the effective Hamiltonian (3) and read

$$\epsilon_\pm(k_x, k_y) = \pm\hbar\kappa \left[J_0^2(\Gamma_1) + J_0^2(\Gamma_2) + J_0^2(\Gamma_3) + 2J_0(\Gamma_1)J_0(\Gamma_2) f_1 \right.$$
$$\left. + 2J_0(\Gamma_1)J_0(\Gamma_3) f_2 + 2J_0(\Gamma_2)J_0(\Gamma_3) f_3 \right]^{\frac{1}{2}}, \tag{11}$$

where we have set

$$f_1 = \cos(\sqrt{3}ak_y), \tag{12}$$

$$f_2 = \cos\left[\left(\frac{\sqrt{3}}{2} k_y + \frac{3}{2} k_x \right) a - \frac{ea A_x \sin\varphi}{\hbar\omega} \right], \tag{13}$$

$$f_3 = \cos\left[\left(-\frac{\sqrt{3}}{2} k_y + \frac{3}{2} k_x \right) a - \frac{ea A_x \sin\varphi}{\hbar\omega} \right] \tag{14}$$

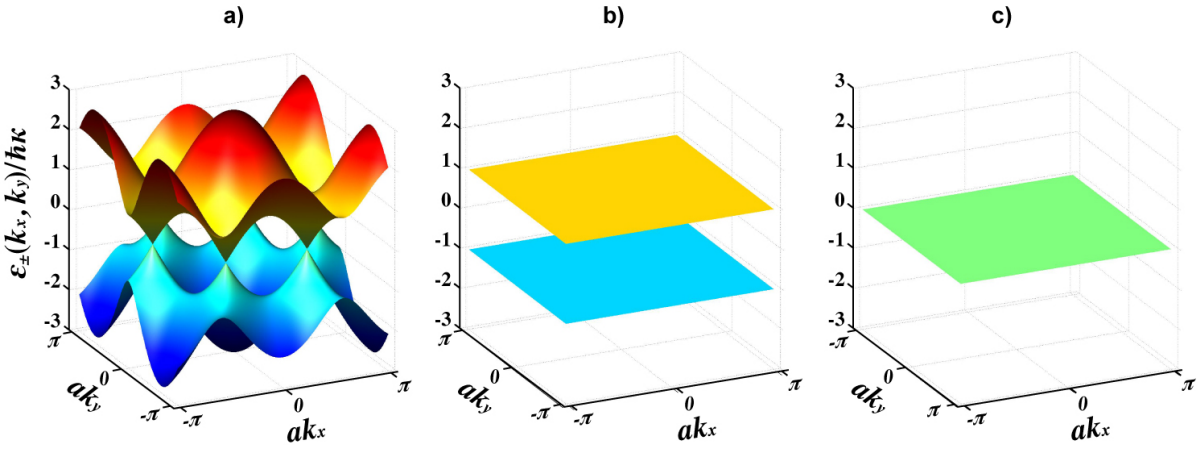

Figure 2. (a) Band structure of graphene in the absence of the external ac field. (b) Partial collapse of the quasi-energies for a linearly-polarized field. (c) Complete collapse for a circularly-polarized field.

and where $\mathbf{k} = k_x\mathbf{u}_x + k_y\mathbf{u}_y$ is the electron quasi-momentum. Equations (11)–(14) generalize, in the case of an arbitrarily polarized ac field, the quasi-energy band calculation previously reported in [15] for graphene in a linearly-polarized field, and enable us to predict the occurrence of partial or complete collapse of valence (ϵ_-) and conduction (ϵ_+) quasi-energy bands depending on the polarization state of the driving field. A partial band collapse is obtained whenever two of the three parameters Γ_1, Γ_2 and Γ_3 are the roots of the J_0 Bessel function, whereas complete band collapse requires that all of them are roots of J_0. Let us apply our results to some specific cases.

1. *Absence of the ac field* ($A_x = A_y = 0$). In this case we obtain the usual band structure of graphene (see figure 2(a)):

$$\epsilon_\pm(k_x, k_y) = \pm\hbar\kappa \sqrt{1 + 4\cos^2\left(\frac{\sqrt{3}ak_y}{2}\right) + 4\cos\left(\frac{\sqrt{3}ak_y}{2}\right)\cos\left(\frac{3ak_x}{2}\right)}. \tag{15}$$

   Note that the two (conduction and valence) bands touch at the Dirac points, where $\epsilon = 0$ and the dispersion relation is locally conical.

2. *Linearly-polarized field along the y-axis* ($A_x = 0$). Under the effect of linear polarization, partial collapse of the quasi-energy bands can be obtained in different ways, depending on the polarization direction. Here we will discuss in detail the example that will actually be implemented in this work. However, all cases can be derived easily from the above equations. For the y-polarized field one has $\Gamma_1 = \Gamma_2 = \sqrt{3}eaA_y/(2\hbar\omega)$ and $\Gamma_3 = 0$. In particular, for $J_0(\Gamma_1) = 0$ one obtains partial collapse of the quasi-energy conduction and valence bands into two flat bands, separated by $2\hbar\kappa$, i.e. $\epsilon_\pm(k_x, k_y) = \pm\hbar\kappa$ (see figure 2(b)). In the effective lattice model of figure 1(b), this case corresponds to the suppression of the hopping rates κ_1 and κ_2, but not κ_3.
3. *Circularly-polarized field* ($A_x = A_y = A_0$, $\varphi = \pi/2$). In this case, $\Gamma_1 = \Gamma_2 = \Gamma_3 = eaA_0/(\hbar\omega)$ and a complete band collapse $\epsilon_\pm(k_x, k_y) \equiv 0$ can be observed whenever

$J_0(\Gamma_1) = 0$ (see figure 2(c)). In this case, we basically destroy all the hopping rates κ_1, κ_2 and κ_3.

It should be noted that complete band collapse by a monochromatic driving field is only achievable in 2D lattices with special symmetries, such as in square, triangular and hexagonal lattices (of which photonic graphene is a relevant example). While in square lattices complete band collapse can be obtained using linearly-polarized fields[2], in honeycomb lattices this is possible using only a circular (or certain elliptical) polarization state of the driving field, as can be inferred from equations (8)–(10). Complete band collapse could be achieved in honeycomb lattices using a linearly-polarized *but highly non-monochromatic* driving field, as demonstrated in [30] for the similar case of a triangular lattice.

3. Ac-driven photonic graphene

Light transport in a honeycomb lattice of evanescently-coupled optical waveguides is known to realize a simple model system of graphene (see, for instance, [22, 24]). The effect of the ac driving field can be mimicked by sinusoidally-bending the optical axis of the waveguides along the paraxial spatial propagation direction z (see, for instance, [33, 34]). Indicating by ψ_n the light field amplitude trapped in the nth waveguide of the honeycomb lattice and considering only the evanescent field coupling of nearest-neighbour waveguides from different sublattices, the evolution of the amplitudes $\psi_n(z)$ along the spatial z direction is described by the following coupled-mode equations [33, 34][3]

$$\mathrm{i}\frac{\mathrm{d}\psi_n}{\mathrm{d}z} = -\kappa \sum_{\langle m \rangle} \psi_m + \frac{2\pi n_\mathrm{s}}{\lambda}\ddot{\mathbf{R}}(z)\cdot\mathbf{r}_n\psi_n, \tag{16}$$

where

$$\mathbf{R}(z) = x_0(z)\mathbf{u}_x + y_0(z)\mathbf{u}_y \tag{17}$$

is the bending profile of the waveguide axis, λ is the wavelength of the optical propagating field, n_s is the refractive index of the dielectric substrate at wavelength λ, and the sum on the right-hand side of equation (16) is restricted to the nearest neighbour waveguides $\langle m \rangle$ of n. Note that the optical coupled-mode equation (16) exactly reproduce the one-particle dynamics as described by the time-dependent tight-binding Hamiltonian (1), provided that the following formal substitutions

$$t \to z, \tag{18}$$

$$h \to \lambda, \tag{19}$$

$$e\mathbf{E}(t) \to n_\mathrm{s}\ddot{\mathbf{R}}(z) \tag{20}$$

[2] Band collapse in a square lattice is a fairly trivial problem, since it is basically equivalent to dynamic localization in a one-dimensional lattice, as already shown in the pioneering work by Dunlap and Kenkre on dynamic localization (see [31]). The experimental demonstration of such a localization regime in a one-dimensional optical waveguide lattice was earlier reported in [38].

[3] The accuracy of equation (16) is established by coupled-mode-theory under paraxial wave approximation for photonic circuits of weakly-coupled and weakly-guiding waveguides, as is the case of our driven photonic lattice (see e.g. [39] and references therein).

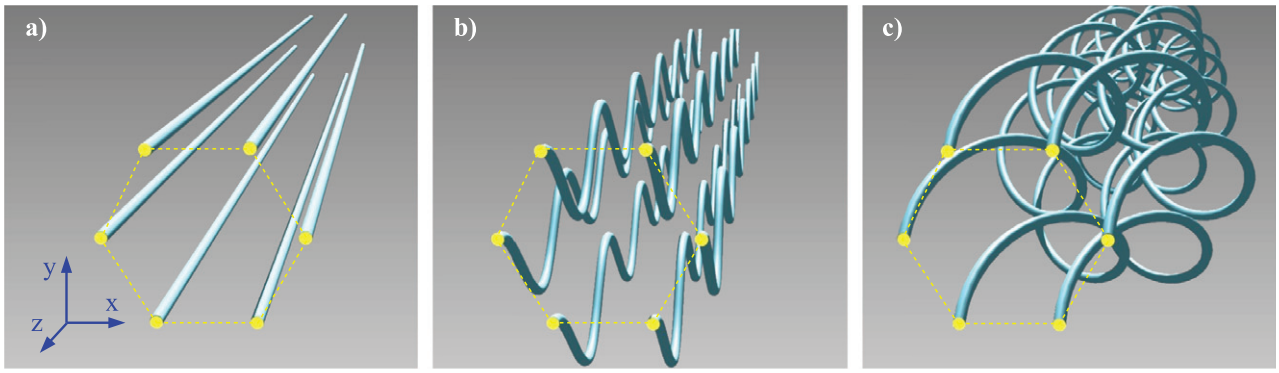

Figure 3. 3D representation of a single hexagonal cell of a honeycomb waveguide array with different modulations of the optical axis: (a) no modulation, (b) sinusoidal modulation along the y-axis and (c) helical modulation.

are made [33]. Hence, the temporal evolution of an electronic wave packet in the ac-driven graphene lattice is mapped into spatial light propagation in the honeycomb waveguide lattice with a bent optical axis.

According to equation (20), the absence of the ac driving field corresponds to a straight waveguide lattice (see figure 3(a)). A sinusoidal driving field linearly-polarized along, for example, the y-axis corresponds to a sinusoidal bending of the optical waveguide axis with a spatial frequency ω in the (y, z) plane, that is $x_0(z) = 0$, $y_0(z) = Y_0 \cos(\omega z)$ (see figure 3(b)). Whereas a sinusoidal and circularly-polarized driving field is mimicked by a helically-bent waveguide axis about the z-axis with a helix spatial frequency ω, that is $x_0(z) = X_0 \cos(\omega z + \pi/2)$, $y_0(z) = Y_0 \cos(\omega z)$ (see figure 3(c)).

In this work, arrays of waveguides with all the three geometries previously discussed and depicted in figure 3 are fabricated by the femtosecond laser writing technique [40, 41]. This technique allows the microfabrication of high-quality optical waveguides in transparent dielectric substrates in a direct fashion. Femtosecond laser pulses are focused by a microscope objective under the sample surface and nonlinear absorption phenomena induce a localized refractive index increase: waveguiding structures with arbitrary 3D geometries can be fabricated by properly translating the sample under the laser beam at a constant speed, along the desired path. It may be noted that the realization of such complex 3D structures as the ones needed here is out of reach for conventional lithographic technologies and is made possible uniquely by femtosecond laser micromachining. The use of femtosecond-laser-written waveguide lattices as photonic models to study hard-to-observe quantum phenomena has already proven to be a feasible and powerful approach (see, for instance, [42, 43]).

In particular, for our experiments, the second harmonic (520 nm wavelength) of a femtosecond laser system (HighQLaser femtoREGEN with pulse duration of 400 fs) is employed to write waveguides on fused silica glass (Foctek, China) through a 50× microscope objective (0.6 NA). Irradiation parameters are optimized to obtain low-loss (1 dB cm^{-1}) single-mode waveguides at 633 nm wavelength, which are capable of bending in three dimensions with bending losses lower than 2 dB cm^{-1} for curvature radii above 80 mm. The chosen irradiation conditions are: 20 kHz repetition rate, 430 nJ pulse energy and 15 mm s^{-1} translation speed.

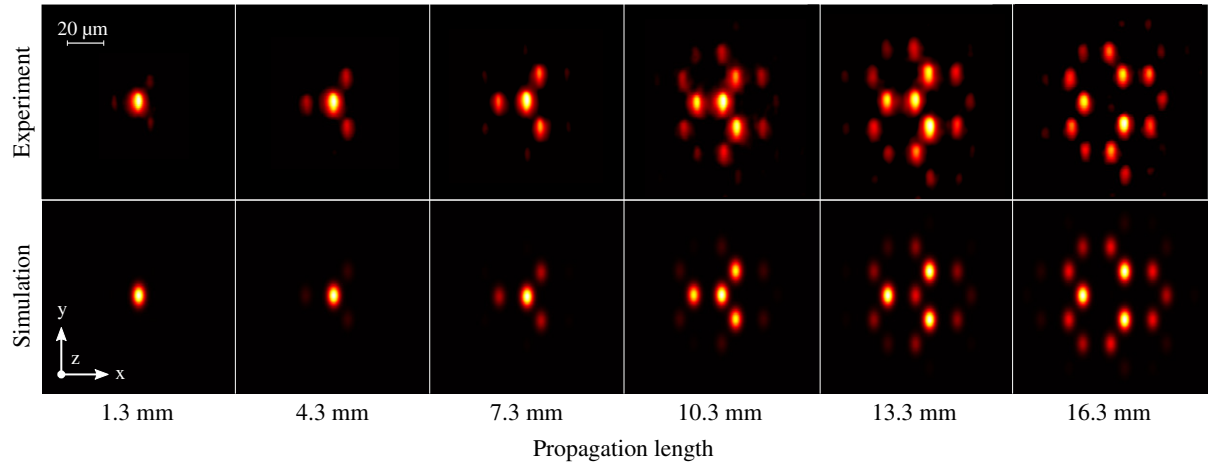

Figure 4. Experimental and simulated output light intensity distributions for honeycomb arrays, comprising 72 straight waveguides, with different propagation lengths.

To obtain accurate control of the geometrical parameters, a system of high-precision micro-translation stages (Aerotech model FiberGlide 3D) was employed. This allowed fabrication at a constant value of the tangential writing speed, which is key to attaining uniform waveguides in complex 3D geometries. The mean depth of the fabricated structures is 170 μm below the sample surface.

4. Experimental results

As a first experiment, several 2D arrays, each composed of 72 straight waveguides in honeycomb geometry, are fabricated in a 2 cm long fused silica sample. In each array, only one waveguide (in central position) covers the full length of the sample: all the others start at a certain distance from the edge, different in each array. In this way, light can be selectively coupled to the central waveguide, avoiding unwanted direct coupling to more than one waveguide, and in addition allowing the investigation on different effective propagation lengths of the arrays without having to cut the same sample many times. The explored propagation lengths range from 1.3 to 16.3 mm and the distance between nearest-neighbouring waveguides is always $a = 15$ μm.

To experimentally characterize the light propagation and distribution in such structures, light at 633 nm wavelength from a 30 mW He:Ne laser is end-fire coupled by a 25× objective (0.5 NA) to the central waveguide. The light distribution at the output of the arrays is imaged by another objective onto a high-sensitivity vidicon camera (see top panels of figure 4). The natural fluorescence emission of femtosecond laser written waveguides in fused silica [44, 45] can also be exploited to obtain a convenient visualization of the light propagation along the array.

As discussed in section 3, these structures mimic diffusion phenomena in graphene lattices. In particular, the initial excitation of a single waveguide of the array corresponds to a

point-like initial distribution. The use of straight waveguides without any modulation represents the absence of external fields. Figure 4 shows the comparison between the experimental light distributions and the corresponding numerical simulations, based on the tight-binding Hamiltonian (equation (16)) in the absence of external fields, for $\kappa = 0.6\,\mathrm{cm}^{-1}$.[4] The numerical results have been obtained by integration of equation (6) with a fourth-order variable-step Runge–Kutta method based on the Dormand–Prince formula [46]. It can be seen that, notwithstanding the weak coupling, light already spreads to several waveguides in less than 2 cm. The good agreement between experimental and simulated distributions assesses the validity of our photonic model for reproducing coherent transport phenomena in honeycomb lattices. In addition, it may be worth noting that, as previously discussed, the top panels in figure 4 correspond to separate waveguide arrays of different lengths, thus testifying to the very good reproducibility of the fabrication technique.

In a second experiment, another two series of arrays with effective propagation lengths ranging from 2 to 14 mm are fabricated. In the first series, the waveguide arrays are sinusoidally modulated along the y-axis, as depicted in figure 3(b). The period of the sinusoid is $\Lambda = 6.30\,\mathrm{mm}$ and the modulation amplitude is $Y_0 = 12.9\ \mu\mathrm{m}$. In the second series, the waveguides have helical geometry, as shown in figure 3(c). The pitch of the helix is again $\Lambda = 6.30\,\mathrm{mm}$ and the radius is $X_0 = Y_0 = 11.2\,\mu\mathrm{m}$. The two kinds of modulation mimic the presence of a strong external oscillating electric field (see section 3), with frequency $\omega = \frac{2\pi}{\Lambda} \simeq 10\,\mathrm{cm}^{-1}$ and linear or circular polarization, respectively. The modulation amplitudes are designed to provide the band-collapse regimes discussed in section 2, and $\omega \gg \kappa$ as assumed in the same section.

The output light distribution is imaged for all the fabricated arrays. In the case of sinusoidally modulated arrays, light coupling is observed only from the input waveguide to the adjacent one in the xz plane: coupling to the other waveguides is negligible. This confirms that, referring to figure 1(b), only κ_3 is still significant, while κ_1 and κ_2 vanish. This result demonstrates the possibility of achieving partial collapse of the quasi-energy bands under the action of linearly-polarized light.

In the case of helically modulated structures, light was observed to remain, for any propagation length, strongly confined in the input waveguide. As theoretically predicted, all the couplings κ_1, κ_2 and κ_3 are effectively suppressed. This demonstrates the possibility of achieving a complete collapse of the quasi-energy bands under the effect of circularly polarized light.

Figure 5 shows top-view fluorescence emission images of the arrays: these confirm the fact that while in the case of an unmodulated array (figure 5(a)) light spreads to several waveguides, in the case of modulated arrays light remains strongly confined to two coupled waveguides (figure 5(b), in the case of sinusoidal modulation) or to a single waveguide (figure 5(c), in the case of helical modulation). Figures 5(d)–(f) show the output distributions of 13.3 mm long arrays in the case of no modulation, sinusoidal modulation and helical modulation, respectively. Figures 5(g)–(i) report the corresponding simulations for $\kappa = 0.6\,\mathrm{cm}^{-1}$. The partial and complete localization effects discussed above are clear and apparent, with good agreement between simulation and experiment.

[4] The ellipticity of the waveguide mode profile induces a slight dependence of the coupling coefficient on the coupling angle in the 2D lattice. This dependence is measured in a 5% variation about the average value given in the text. It should be noted that for the propagation length employed in this experiment, such variation is negligible.

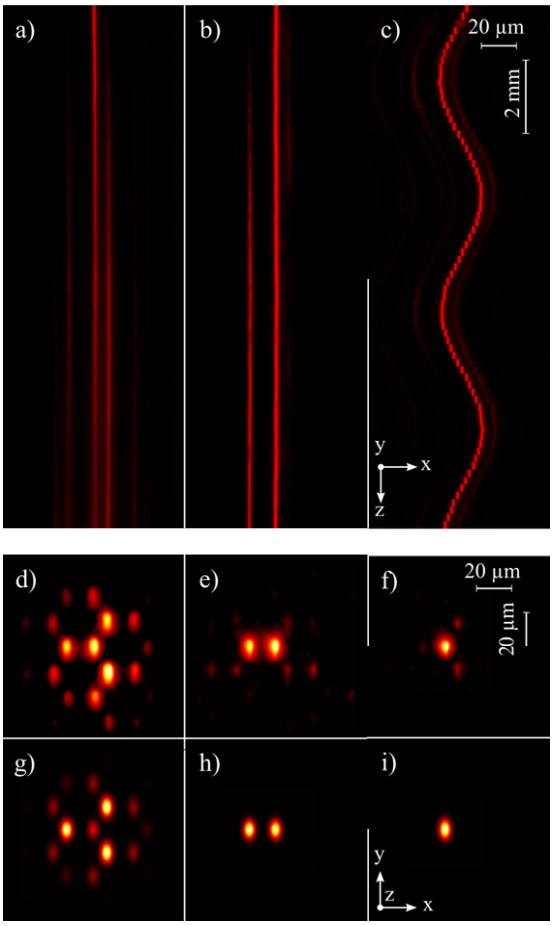

Figure 5. Top view of the fluorescence emission of 13.3 mm long honeycomb arrays of 72 waveguides with (a) no modulation, (b) sinusoidal modulation in y direction to obtain partial quasi-energy band collapse, and (c) helical modulation to obtain complete energy band collapse. Panels (d)–(f) show the corresponding experimental output light intensity distributions; panels (g)–(i) the simulated output distributions.

5. Conclusions

Complete collapse of quasi-energy bands in graphene under the effect of monochromatic circularly-polarized light has been suggested, theoretically investigated and experimentally demonstrated in a photonic model system. Coherent transport phenomena in graphene have been modelled by light propagation in a honeycomb waveguide lattice, called photonic graphene. In the framework of this model, the polarization of the external field is implemented by suitably bending the waveguide axis. Exploiting the unique 3D capabilities of femtosecond laser waveguide writing, not only 2D waveguide arrays, but also sinusoidally and helically modulated arrays have been fabricated, representing monochromatic linearly- and circularly-polarized fields, respectively, applied to graphene. Observation of the light distribution in such structures clearly demonstrated partial and complete band collapse. These results suggest an

innovative approach to performing coherent band-engineering of graphene by irradiation with monochromatic light of suitable polarization.

Acknowledgments

This work is partially funded by the European Commission under the 7th Framework Programme through the project QWAD-*Quantum Waveguides Application and Development* (FP7-ICT-2011-9-600838).

References

[1] See for instance, Das Sarma S, Adam S and Hwang E H 2011 *Rev. Mod. Phys.* **83** 407
[2] Katsnelson M I, Novoselov K S and Geim A K 2006 *Nature Phys.* **2** 620
[3] Stander N, Huard B and Goldhaber-Gordon D 2009 *Phys. Rev. Lett.* **102** 026807
[4] Trauzettel B, Blanter Y M and Morpurgo A F 2007 *Phys. Rev.* B **75** 035305
[5] Fistul M V and Efetov K B 2007 *Phys. Rev. Lett.* **98** 256803
[6] Syzranov S V, Fistul M V and Efetov K B 2008 *Phys. Rev.* B **78** 045407
[7] Oka T and Aoki H 2009 *Phys. Rev.* B **79** 081406
[8] Kibis O V 2010 *Phys. Rev.* B **81** 165433
[9] Abergel D S L and Chakraborty T 2009 *Appl. Phys. Lett.* **95** 062107
[10] Abergel D S L and Chakraborty T 2011 *Nanotechnology* **22** 015203
[11] Kitagawa T, Oka T, Brataas A, Fu L and Demler E 2011 *Phys. Rev.* B **84** 235108
[12] Calvo H L, Pastawski H W, Roche S and Foa Torres L E F 2011 *Appl. Phys. Lett.* **98** 232103
[13] Lopez-Rodriguez F J and Naumis G G 2008 *Phys. Rev.* B **78** 201406
[14] Rivera P H, Pereira A L C and Schulz P A 2009 *Phys. Rev.* B **79** 205406
[15] Zhang W, Zhang P, Duan S and Geng Zhao X 2009 *New J. Phys.* **11** 063032
[16] Zhou Y and Wu M W 2011 *Phys. Rev.* B **83** 245436
[17] Wu B H, Liu Q, Jiang X and Cao J C 2012 *Appl. Phys. Lett.* **100** 203106
[18] Busl M, Platero G and Jauho A P 2012 *Phys. Rev.* B **85** 155449
[19] Wu C and Das Sarma S 2008 *Phys. Rev.* B **77** 235107
[20] Juzeliünas G, Ruseckas J, Lindberg M, Santos L and Öhberg P 2008 *Phys. Rev.* A **77** 011802
[21] Tarruell L, Greif D, Uehlinger T, Jotzu G and Esslinger T 2012 *Nature* **483** 302
[22] Peleg O, Bartal G, Freedman B, Manela O, Segev M and Christodoulides D N 2007 *Phys. Rev. Lett.* **98** 103901
[23] Zhang X 2008 *Phys. Rev. Lett.* **100** 113903
[24] Bahat-Treidel O, Peleg O, Grobman M, Shapira N, Segev M and Pereg-Barnea T 2010 *Phys. Rev. Lett.* **104** 063901
[25] Zandbergen S R and de Dood M J A 2010 *Phys. Rev. Lett.* **104** 043903
[26] Huang X, Lai Y, Hang Z H, Zheng H and Chan C T 2011 *Nature Mater.* **10** 582
[27] Torrent D and Sanchez-Dehesa J 2012 *Phys. Rev. Lett.* **108** 174301
[28] Szameit A, Garanovich I L, Heinrich M, Sukhorukov A A, Dreisow F, Pertsch T, Nolte S, Tünnermann A and Kivshar Y S 2009 *Nature Phys.* **5** 271
[29] Zenesini A, Lignier H, Ciampini D, Morsch O and Arimondo E 2009 *Phys. Rev. Lett.* **102** 100403
[30] Szameit A, Garanovich I L, Heinrich M, Sukhorukov A A, Dreisow F, Pertsch T, Nolte S, Tünnermann A, Longhi S and Kivshar Y S 2010 *Phys. Rev. Lett.* **104** 223903
[31] Dunlap D H and Kenkre V M 1986 *Phys. Rev.* B **34** 3625
[32] Holthaus M 1992 *Phys. Rev. Lett.* **69** 351
[33] Longhi S 2009 *Laser Photon. Rev.* **3** 243
[34] Garanovich I L, Longhi S, Sukhorukov A A and Kivshar Y S 2012 *Phys. Rep.* **518** 1

[35] Jia S and Fleischer J W 2009 *Phys. Rev.* A **79** 041804
[36] Eckardt A, Weiss C and Holthaus M 2005 *Phys. Rev. Lett.* **95** 260404
[37] Creffield C E 2007 *Phys. Rev. Lett.* **99** 110501
[38] Longhi S, Marangoni M, Lobino M, Ramponi R, Laporta P, Cianci E and Foglietti V 2006 *Phys. Rev. Lett.* **96** 243901
[39] Huang W-P 1994 *J. Opt. Soc. Am.* A **11** 963
[40] Della Valle G, Osellame R and Laporta P 2009 *J. Opt. A: Pure Appl. Opt.* **11** 013001
[41] Ams M, Marshall G, Dekker P, Piper J and Withford M 2009 *Laser Photon. Rev.* **3** 535–44
[42] Crespi A, Longhi S and Osellame R 2012 *Phys. Rev. Lett.* **108** 163601
[43] Zeuner J M, Efremidis N K, Keil R, Dreisow F, Christodoulides D N, Tünnermann A, Nolte S and Szameit A 2012 *Phys. Rev. Lett.* **109** 023602W
[44] Szameit A, Dreisow F, Hartung H, Nolte S, Tünnermann A and Lederer F 2007 *Appl. Phys. Lett.* **90** 241113
[45] Szameit A and Nolte S 2010 *J. Phys. B: At. Mol. Opt. Phys.* **43** 163001
[46] Dormand J R and Prince P J 1980 *J. Comput. Appl. Math.* **6** 19